2023 IEEE International Conference on Robotics and Automation (ICRA 2023)
May 29 - June 2, 2023. London, UK

A Soft Robot with Three Dimensional Shape Sensing and Contact Recognition Multi-Modal Sensing via Tunable Soft Optical Sensors*

Max McCandless†, Frank Juliá Wise†, and Sheila Russo‡

***Abstract*— Soft optical sensing strategies are rapidly developing for soft robotic systems as a means to increase the controllability of soft compliant robots. In this paper, we present a roughness tuning strategy for the fabrication of soft optical sensors to achieve the dual functionality of shape sensing combined with contact recognition within a single multi-modal sensor. The molds used to fabricate the soft sensors are roughened via laser micromachining to achieve asymmetrical sensor responses when bent in opposite directions. We demonstrate the integration of these sensors into a fully soft robotic platform consisting of a multi-directional bending module with integrated 3D shape sensing and a gripper with tip position monitoring along with contact force recognition. We show the accuracy of our sensing strategy in validation experiments and a pick-and-place task is performed to demonstrate the robot's functionality.**

I. Introduction

The design, control, and functionality of soft robotic manipulators and grippers are growing areas of research interest [1], [2]. Recent advancements in soft grippers enhance gripper strength and adhesion [3], grasping reliability [4], and open-loop control [5]. Presently, research is pushing toward closed-loop control via embedding proprioceptive and contact force sensors into soft grippers [6]. Sensing technologies explored include resistive and capacitive for haptic feedback [7], [8], liquid metal strain sensors [9], visual servoing for shape sensing and vision-based tactile sensing [10]–[12], electro-conductive shape sensing yarn [13], magnetic sensing for bidirectional proprioception [14], and optical sensors for movement detection [15]. Optical technology provides many opportunities to embed sensor feedback into soft morphable and compliant robots [16], [17], e.g., shape sensing and contact force recognition [18]–[20]. Fully soft optical sensors proved useful from a sensor characteristic standpoint, where highly lossy soft waveguides can be exploited [21]. These sensors have been used within soft robots to measure elongation, strain, bending, shape, contact forces, and blood detection [22]–[26]. Robotic grippers and hands incorporate optical sensing for contact force sensitivity and location [27]–[29] and to monitor bending [30], [31]. The development and integration of soft optical sensing can benefit from designing tuned sensor responses. Researchers have tuned the roughness of an acrylic optical fiber to see optical gains through a single bending direction of an optical waveguide for a soft orthotic device [32]. Another sensor combines commercially available soft and selectively scratched flexible rigid fibers to differentiate sensor loss modes [33]. However, these sensors are not fully soft, thus presenting limitations when integrated with soft robots. Fully soft sensing capabilities allow for sensing to be embedded into soft robots without adversely affecting the compliant nature, flexibility, or range of motion of the systems. As compared to other fully soft shape sensing strategies, such as resistive and pressure, optical sensors present the opportunity to accurately predict shape and contact force interactions with less total sensor inputs required, and thus less external connections [34], [35]. To develop a complete robotic platform, soft robotic grippers are often attached to rigid robot arms [7], [36]. These grippers embed sensing for proprioceptive and exteroceptive capabilities. However, the need to attach these systems to rigid robotic arms highlights the need for shape sensing continuum robots [37]. Soft optically sensorized continuum modules capable of shape, curvature, and tip position sensing have been developed without integrated grasping capabilities [22], [38]. Combining fully soft shape sensing continuum robots and grippers into a complete system pushes toward the future of accurate closed-loop control of soft robotic platforms.

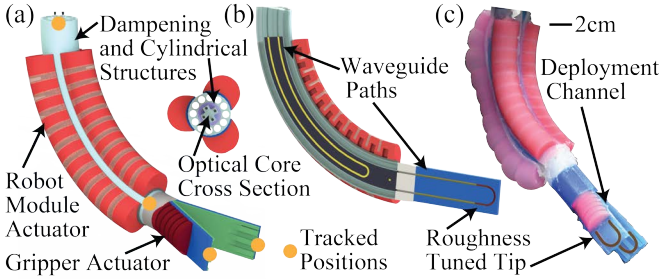

Fig. 1. An optically sensorized soft robot consisting of a 3D shape sensing module connected to a soft robotic gripper capable of tip location sensing and contact force recognition. a) CAD of the robot and top view showing the tracked positions of the device. b) A cross sectional view showing the embedded soft optical sensor paths. c) Fabricated device highlighting the roughened tip for multi-modal sensing of the gripper.

This paper presents a fully soft robot combining *i)* a soft optical sensorized multi-modal gripper for tip tracking and contact recognition with *ii)* a multi-directional bending module with integrated 3D shape sensing (Fig. 1). The gripper embeds two soft pneumatic actuators to deploy the gripper, two soft pneumatic actuators to control grasping, and two soft optical waveguides (one in each jaw of the gripper) with tuned roughness to monitor both actuator tip positions and subsequent occurrence of contact with an object. Prior works on multi-modal response with a single optical sensor

*Research reported in this publication was supported by the National Institute of Biomedical Imaging and Bioengineering of the NIH under award number R21EB029154. The content is solely the responsibility of the authors and does not necessarily represent the official views of the NIH.

The authors are with the Department of Mechanical Engineering, Boston University, Boston, Massachusetts 02215.

†These authors contributed equally to this work.

‡Corresponding author. E-mail: russos@bu.edu.

have explored RGB light monitoring of a dual-core doped sensor or using a gold layer on a set of waveguides to limit scattering losses and tune the sensor response [39]–[41]. In this work, we tune the response of these soft optical waveguide sensors (WG) by tuning the roughness of the molds used to fabricate them. The roughness tuning generates selectively anisotropic WGs which are used to develop 3D shape sensing with distinctly bidirectional WG responses (optical gain and optical loss in either opposite direction). Three soft pneumatic actuators are integrated to steer the robot tip in all directions, and constant curvature modeling is used for mapping the robot workspace [42]. The WG signals are calibrated and fit to multiple surface mappings that are switched between during real-time shape sensing and contact recognition.

II. Materials and Methods

The robot module and gripper contain embedded WGs with 1 mm^2 cross sections. The 125 mm long module contains two perpendicular WG cross sections embedded in a "U" shape with radii of curvature of r = 3 mm and lengths of 91 mm and 107 mm (Fig. 1, b). These cross sections are encased in an 11 mm diameter cylindrical structure designed to both prevent buckling during bending and sensor interference from actuator inflation (Fig. 1, a). The cylindrical structure is encapsulated in a 20 mm diameter strain dampening structure which incorporates 12 equally spaced 3 mm diameter air channels that reduce the stiffness of the system while dampening strains on the robot structure to further prevent adverse effects of actuator expansion on the WG responses (Fig. 1, a). Three PneuNet actuators are spaced 120° apart and are each bonded to the dampening structure with an additional 0.9 mm strain limiting layer (Fig. 1, a). The 50 mm long gripper consists of two jaws each with a PneuNet actuator and a single "U" shaped 43 mm long WG with radius of curvature of r = 5 mm (Fig. 1, b). The 17 mm end tip of the gripper sensor has a laser tuned surface roughness (Fig. 1, c). The gripper is initially closed and deploys (opens jaws) via two air channels located at the base of its innermost layer (one in each half) (Fig. 1, c). The actuators do not extend to the distal end of the gripper. The distal tip is thus free to bend in the opposite direction of the actuator expansion upon contact with an object, which will occur on the portion of the WG that has embedded surface roughness tuning characteristics. The tuning of the WG response allows for the dual functionality of the single embedded WG to provide tip position sensing and contact force recognition upon interacting with an object.

The WGs consist of an optical cladding layer made with Mold Star™ 30 (Smooth-On), with refractive index n_2 = 1.40, and a core of Norland Optical Adhesive 73 (NOA 73), with refractive index n_1 = 1.56. This defines an angle of total internal reflection θ_c of 63.8°, as determined by: $\theta_c = sin^{-1}(n_2/n_1)$. A red 650 nm LED (IF-E99B, Industrial Fiber Optics [IFO]) is utilized as a light source emitter. An infrared spectrum phototransistor (IF-D92, IFO) monitors the optical power through the device. Light is coupled through a 1 mm diameter plastic optical fiber (POF) (GH4001, IFO).

A. Soft Robotic Platform Fabrication

1) Robot Module Fabrication: The robot module's WGs are manufactured by molding into computer numerical control (CNC) fabricated molds (two flat base molds and two molds with the WG channels). The molds are filled with Mold Star™ 30, degassed, and cured (Fig. 2, a_1). The two sets (one base and one WG channel) are bonded together (Fig. 2, a_2) and trimmed into the shape shown in Fig. 2, a_{3-4}. The WGs are slotted together into the cross structure shown in Fig. 2, b_1 and are placed in a 3D-printed (Formlabs grey standard resin, Form2 SLA 3D-Printer) jig to hold them in an upright configuration. Mold Star™ 30 is injected to bond them together. Each WG is placed in a second mold with 1 mm pins into its core and Dragon Skin™ 30 (Smooth-On) is poured over the end (to generate a stiff end cap for POF integration) and cured (Fig. 2, b_2). The pins are removed and NOA 73 is injected into each sensor core channel. The POFs are interfaced with the uncured optical core material. The core material is UV cured using a UVITRON SunSpot 2 light for 3 min. This entire cross section is placed into a 3D printed jig to create the cylindrical anti-buckling structure out of Mold Star™ 30 (Fig. 2, b_{3-4}). Twelve 3 mm pins are slotted into the 3D-printed strain dampening structure mold and an outer shell is placed around the pins (Fig. 2, c_1). Ecoflex™ 00-30 (Smooth-On) is poured into the mold to create the strain dampening structure. The pins are removed and the entire device is demolded (Fig. 2, c_2). PneuNet actuators are fabricated using Dragon Skin™ 10 MEDIUM (Smooth-On) in 3D printed molds (Fig. 2, d_1) with a Dragon Skin™ 30 strain limiting layer (Fig. 2, d_2). The channels between the PnueNet structure are filled with Ecoflex™ 00-50 (Fig. 2, d_3). The three actuators are bonded to the dampening structure and tubing is inserted (Fig. 2, e).

2) Gripper Fabrication: The gripper's WGs are manufactured by molding into CNC molds with a surface roughness defined by the tool cut, i.e., "as machined" roughness (Fig. 2, f). The roughness of the top surface of the tip (front third) portion of the "U" shaped feature is tuned via laser micromachining (see Sect. II-B.1). Mold Star™ 30 is poured into the WG molds, degassed, and cured. Ecoflex™ 00-30 is poured into the air channel layer molds (deployment actuator and jaw molds), degassed, and cured (Fig. 2, g). The PnueNet bending actuators are fabricated using Dragon Skin™ 30 (Fig. 2, h). The actuator molds are then bonded to the WGs. These steps (Fig. 2, f-h) are repeated to make the two halves of the gripper. The injection of the WG cores follows the same procedure as in Sect. II-A.1. The gripper is assembled (Fig. 2, i) and combined with the robot module and the actuation and sensor cables are routed through the dampening structure (Fig. 1, c).

B. Roughness Tuning and Soft Sensor Physics

1) Roughness Tuning: A laser (Coherent Matrix 355 nm laser precision micromachining system, 5 W) was used to tune the roughness of the aluminum molds for the gripper's

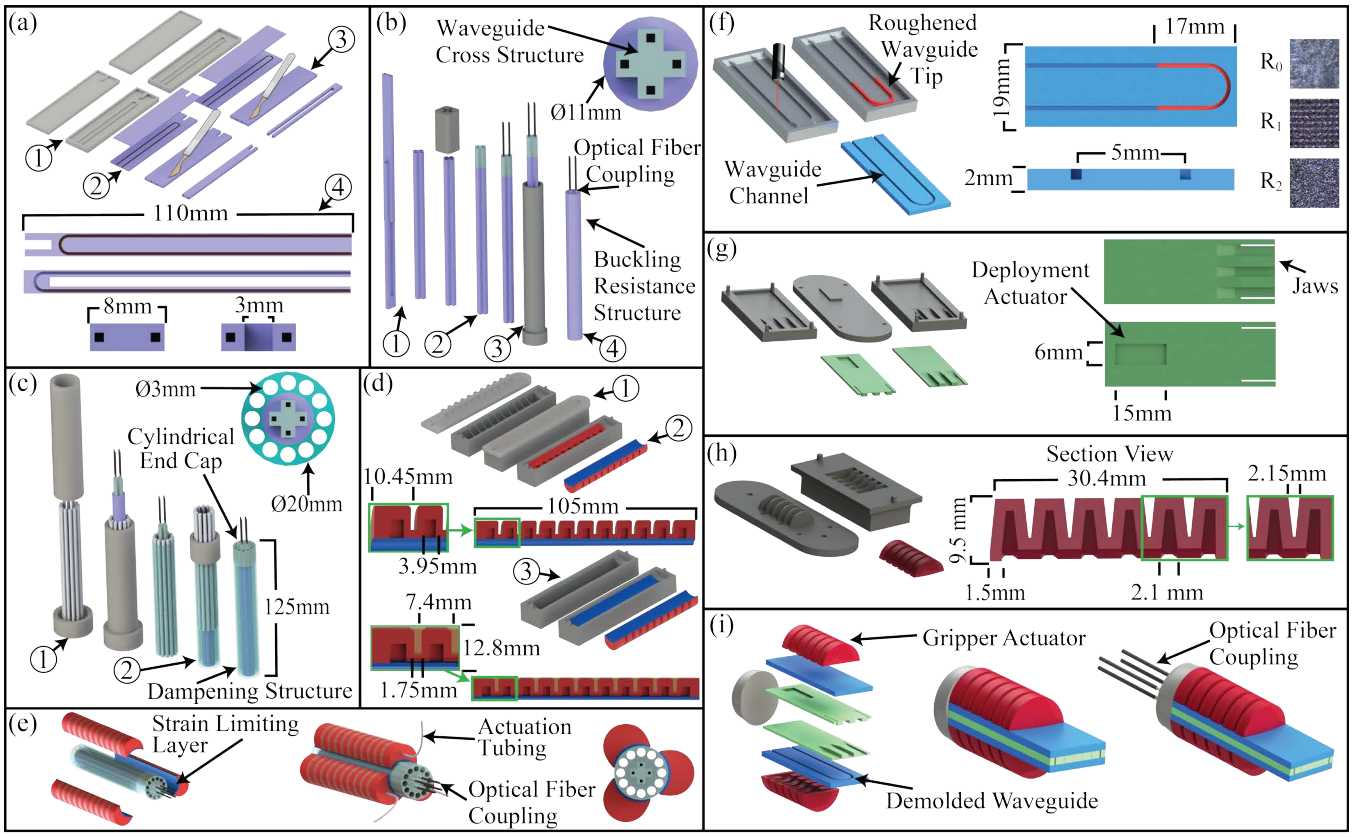

Fig. 2. Soft robot fabrication. Robot module fabrication (a-e) and gripper fabrication (f-i). a) WGs embedded in the cross structure of the robot module. b) Cross structure assembly and molding into a cylindrical shape. c) Dampening structure around the sensing core. d) Pneumatic actuators molding. e) 120° spaced actuators placed on the dampening structure. f) Roughness tuned molds and microscope images of the surface roughnesses. g) Molds for the deployment actuation channel and the gripper jaws. h) Molds for gripper bending actuators. i) Gripper assembly.

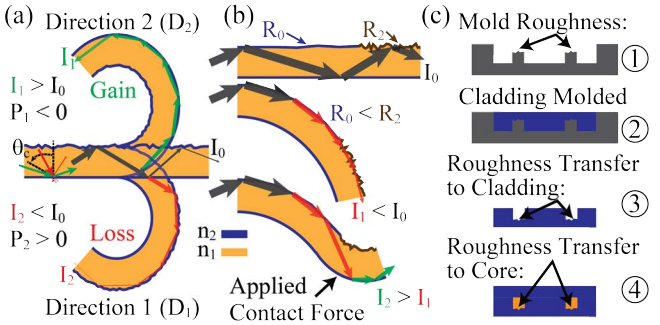

Fig. 3. Sensor response physical principle and roughness tuning. The loss of subsequent rays is shown by shrinking the size of arrow line thickness. a) Light reflecting off of the smoother side (D_2) creating optical gain and the rougher side (D_1) creating optical loss during bending. b) Light intensity change due to an applied contact force on the tip of a roughened sensor causing bending in the opposite direction. c) Diagram of the roughness transfer from the molds to the sensor core and cladding.

WGs with different rastering patterns (Fig. 2, f). The resulting surface roughness values were measured using a coherence scanning interferometer (Zygo NewView 6200 Optical Profiler) to determine the root mean square (S_q) roughness. A cross hatch rastering pattern produces the most ergodic surface finish and thus was chosen as a constant in the roughness values that were ultimately tested on our WGs. Of the roughness values fabricated, three are depicted in subsequent testing experiments (Sect. IV-A.2 and Sect. IV-A.3): the machined roughness R_0 (S_q = 0.179 μm, SD = 0.026 μm), roughness R_1 (S_q = 3.52 μm, SD = 0.404 μm), and roughness R_2 (S_q = 1.96 μm, SD = 0.274 μm). These values were chosen to show the roughness tuning effects of an ideally (R_2) and overly (R_1) roughened sensor compared to a sensor fabricated without roughness tuning (R_0).

2) Sensor Physics: As the module bends and the gripper deploys, bends, and contacts an object, the WGs will exhibit light intensity changes or losses in optical power. The bending of the WG alters the angles of incident light reflecting within the system and which surface the light rays reflect off of the most (inner or outer surface of the core region in the bending plane) (Fig. 3, a). This signal is different when the WG is bent toward (optical gain I_1) or away (optical loss I_2) from the roughened half of the WG as: $I_1 > I_0 > I_2$. The output power change (P) is determined from the WG output power in an undeformed state, i.e., baseline signal (I_0) and the current measured signal (I) as:

$$P = 10 \cdot log_{10}(I_o/I) \quad (1)$$

where $P > 0$ corresponds to a drop in light intensity and $P < 0$ corresponds to an increase in light intensity or decrease in sensor loss. The WGs exhibit distinctly anisotropic behavior as a result of the roughness imparted on the CNC molds. Fig. 3, c depicts the process in which the roughness is transferred onto the WG core and cladding surfaces. Fig. 3, b shows a case where the roughness is modified along the length of a WG. The resulting loss mode changes depending on which section of the WG is bent. This principle is used to generate multi-modal sensing in the soft robotic gripper. We

tune the response to have sensor loss upon bending, but upon contact, the tip of the device is bent in the opposite direction and the increase in light intensity from light rays reflecting on the smooth section more often along the roughened tip results in an increase in the signal: $I_0 > I_2 > I_1$.

III. Experiments

A. Calibration

The calibration of the robot module used a Python program to control and acquire data from three syringe pumps (Pump 11 Pico Plus Elite, Harvard Apparatus) pressurizing the soft actuators, an electromagnetic (EM) tracker (NDI Aurora), and the WG signals via a DAQ (NI USB-6002). The robot module was programmed to move through its entire workspace (up to a max curvature of 10 m^{-1}) while stopping at set points to collect the robot module WG responses (P_1, P_2) and the absolute position of the module tip (from the EM tracker). An EM probe was placed at the robot base and another at its distal tip to determine the tip position during calibration. The x, y, z position of the tip from the tracker is used to determine the r and ϕ in the constant curvature model (Fig. 4). The baseline sensor signal is in the undeformed state, not pressurized, hanging vertically with the tip below the base (Fig. 5, a). From the diagram in Fig. 4, we can derive:

$$\phi = tan^{-1}\left(\frac{y}{x}\right), \quad r = \frac{\ell}{\theta} \tag{2}$$

where $\theta = f(x, y, z)$ is defined by using simple trigonometric rules and the known length of the sensor ℓ can be plugged into the arc length equation (Eq. 2). We can thus map P_1 and P_2 with the robot's r and ϕ at each location within the workspace. Example surface mappings (S) for r and ϕ are shown in Fig. 4.

The calibration of the gripper was conducted with a DAQ to acquire sensor data and camera (Nikon D7500) images analyzed in MATLAB (Mathworks, USA). The gripper's WGs were calibrated in three separate tests by collecting the responses at different deployment angles (α), bending angles (β_1, β_2), and upon contact. First, the WG responses for each half of the gripper (P_3, P_4) are summed and plotted versus deployment angle. Then, the WG responses were monitored versus tip positions following deployment. Lastly, the WG signals are monitored upon contact with an object to develop the control logic for contact force recognition.

B. Testing and Control Platforms

1) Robot Module Control: The calibration of the robot module yields four unique surface mappings for both r and ϕ depending on the optical loss profiles of the WGs, i.e., gain ($P < 0$) or loss ($P > 0$), see Sect. II-B.2, as follows:

$$P_1, P_2 \implies \begin{cases} S_{r_1}, S_{\phi_1} & \text{if } P_1 < 0,\ P_2 < 0 \\ S_{r_2}, S_{\phi_2} & \text{if } P_1 < 0,\ P_2 > 0 \\ S_{r_3}, S_{\phi_3} & \text{if } P_1 > 0,\ P_2 > 0 \\ S_{r_4}, S_{\phi_4} & \text{if } P_1 > 0,\ P_2 < 0 \end{cases} \tag{3}$$

for example, when $P_1 < 0$, $P_2 < 0$ (mapping to S_1), $r = S_{r_1}(P_1, P_2)$ and $\phi = S_{\phi_1}(P_1, P_2)$ and the values of r and ϕ can be determined from the calibrated surface maps such as the examples shown in Fig. 4.

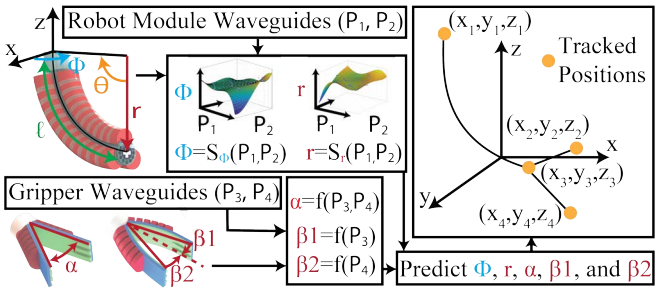

Fig. 4. Flowchart of the calibration and control of the shape sensing robot module and gripper defining the constant curvature variables (r and ϕ) and deployment (α) and bending (β_1 *and* β_2) gripper angles.

2) Roughness Tuning Curvature Testing: To test the bidirectional loss characteristics of the WGs with tuned roughness (see Sect. II-B.1), the WGs were subjected to bending along 3D-printed jigs of set curvatures up to 40 m^{-1}.

3) Gripper Control: To calibrate the gripper, we correlate the signals from the two WGs embedded in each jaw with the deployment angle (α) using a polynomial function that results from the calibration fit as follows:

$$\alpha = f[P_3(I_{0,3}, I_3), P_4(I_{0,4}, I_4)]. \tag{4}$$

From the deployed position, we reestablish a new baseline at the deployment angle I_{0_α} and monitor the subsequent WGs response to track the bending angles β_1 and β_2. A new baseline (I_0) must be established at the set deployment angle for each sensor such that the measured P at the set deployment is based off of I_{0_α}, rather than I_0 (recall Eq. 1):

$$\beta_1 = g_1[P_{3_\alpha}(I_{0_\alpha,3}, I_3)], \quad \beta_2 = g_2[P_{4_\alpha}(I_{0_\alpha,4}, I_4)]. \tag{5}$$

To monitor contact, we compare the change between WG response over the last n data points (determined by a calibrated time interval) until the change of the last n points are all negative (signalling optical gain in the system). The equation to represent this sensor reading change that signals contact is: $\Delta P = P_n - P_{n-1}$ where n is the most recent data point in the log. After we recognize contact has been made and subsequently finish picking up and moving the object, the gripper returns to its deployed state (I_{0_α}) and monitors for contact detection again upon subsequent bending actuation, or the system can fully reset back to its baseline state (I_0).

4) Robot Platform Experiment: A graphical user interface (GUI) was developed to implement the system calibrations and output the real-time shape sensing and contact force recognition of the system. In the experiment, the device is moved through its workspace, picks up an object, and carries it to another location. The WG predicted tracked positions marked in Fig. 1, a and Fig. 4 are output during the test.

IV. Results and Discussion

A. Soft Sensors Characterizations

1) Soft Robot Calibration and Workspace: Fig. 5, b shows the 3D plot of the workspace calibration. The data was sorted into unique surfaces based on the WGs responses and filtered into the four surface mappings (see Eq. 3, Sect. III-B.1), as shown in Fig. 5, a-b. Following the calibration, polynomial equations were developed to map the data to the surfaces in our control accuracy experiments shown in Fig. 5, c-e. The fit order of the polynomial with the minimum error is chosen

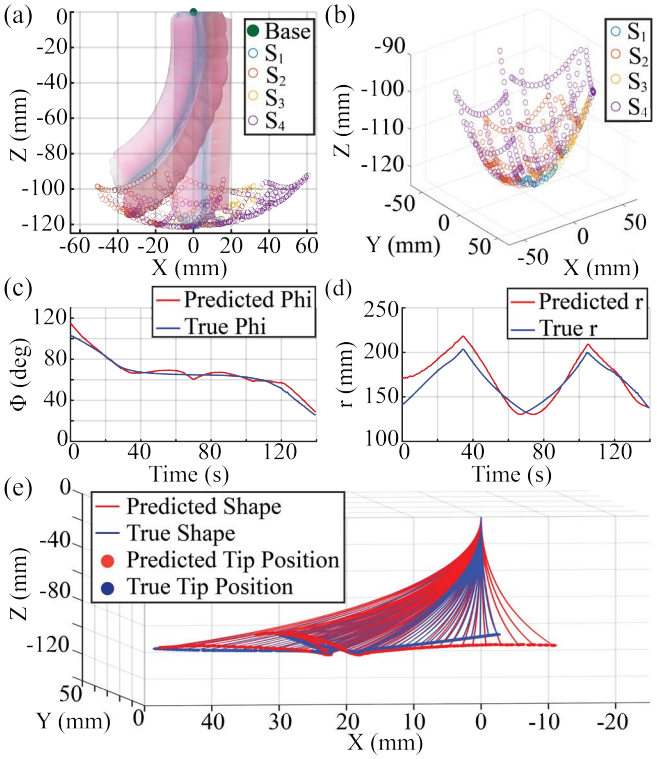

Fig. 5. Module characterizations. a) Calibration example in a single bending orientation and direction. b) Robot workspace mapped into four unique surfaces. Comparison of the true and predicted c) angle ϕ and d) radius of curvature r. e) Predicted and measured shape and tip position (data subset).

for each mapping. In the range tested, the R^2 fit of both the surface of ϕ and r is 0.97. Fig. 5, c and Fig. 5, d compare the true position to the predicted position of ϕ and r. The entire 3D projection of the tip position of the robot module compared to the true position had an average error of 3.4 mm, which is 2.7 % of the length of the system (Fig. 5, e).

2) Surface Roughness Tuning: The three roughness tested for bidirectional curvature sensitivity are shown in Fig. 6, a. In an unbent configuration, the larger the surface roughness value, the lower the baseline light transmittance (I_0). The largest roughness device (R_1) exhibits large optical gains when bending in Direction 2 (D_2 in Fig. 3, a) due to the large difference between the roughened and the smooth side. In contrast, when bending in Direction 1 (D_1), where light tends to reflect more often on the roughened side of the core, the optical loss exhibits minimal sensitivity as no light is able to pass through the core after a curvature of 5 m^{-1}. In comparison, the "as machined" (R_0) WG exhibits optical losses up to ≈1.5 dB/cm at 40 m^{-1}. The R_0 exhibits optical gains up to 10 m^{-1} where-after the light intensity change mode becomes loss for the remainder of the bending (see zoomed in section of the data in Fig. 6, b). In contrast, the WG with tuned roughness R_2 shows increase in optical gain through the entire curvature range (D_2) and also optical losses through the entire curvature range (D_1), i.e., there is no repeated optical power output (P) values in either direction. This ideal functionality is apparent in Fig. 6, b where the difference between the response of R_0 and R_2 is highlighted.

3) Multi-modal Sensing Gripper Characterization and Control Experiments: This section covers the full range of

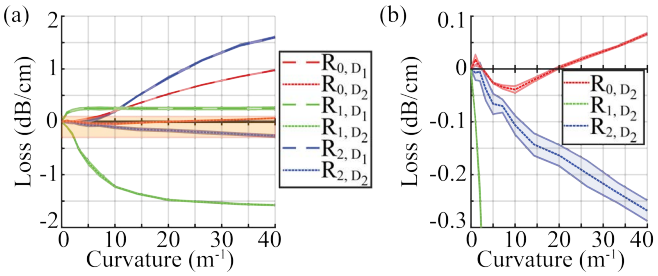

Fig. 6. Surface roughness tunability experimental results. a) The response of the sensors with different roughness is depicted with R_2 yielding the desired response (discrete non-repeating sensor response across the full range of curvatures in both directions). b) A zoomed in portion of the data (orange region from part (a)). The solid line is the mean value and the shaded area is one standard deviation.

testing of the WG signal responses of the robotic gripper and compares the calibration of an ideally roughened gripper (R_2) to a gripper without roughness tuning characteristics embedded (R_0) and one with an excessive roughness (R_1). The ideally roughened device properly balances the loss modes of the sensors and allows for a single sensor unit to predict bending position and recognize contact interactions (multi-modal). See Eq. 4 and Eq. 5 in Sect. III-B.3.

a) Deployment Angle Characterization: The sensor responses versus the deployment angle (α) of each gripper are shown in Fig. 7, a. Each tested gripper was deployed and expanded up to 40° (see inset of Fig. 7, a). Individually, each gripper responded consistently between trials and a polynomial fit was used to generate the equation used in the subsequent control and tip prediction (Sect. IV-A.3.e).

b) Bending Angle Characterization: Following the deployment of the gripper, the subsequent sensor loss is measured while the gripper is closing (Fig. 7, b). Three grippers with embedded WGs with different roughness (R_0, R_1, and R_2) were tested three times and the total change in the angle tested was 40° (β_1 + β_2) (see inset of Fig. 7, b). The overly roughened sensor (R_1) shows the largest loss as curvature is the dominant loss mode. Each bending profile was calibrated and a polynomial fit was used to predict the bending angle in subsequent controls experiments (Sect. IV-A.3.e).

c) Contact Response Characterization: The ideally roughened gripper (R_2) shows an increase in light intensity when contacting an object (Fig. 7, c). This contrasts from the response of R_0 and R_1 where signal loss is measured instead. This provides the ability of the ideally roughened gripper to switch on and sense contact when the light intensity increases. The other grippers would instead predict incorrect bending angles post contacting an object, rather than exhibiting the desired multi-modal response that distinguishes contact from bending with a single sensor.

d) Gripper Multi-Modal Sensing Validation: In Fig. 7, d, the sensor response of the ideal gripper (R_2) is shown in contact and no-contact (bending only) scenarios. The test is carried out in stages and the input to the gripper actuators is identical in both scenarios: deployment (0-37 s), bending to close the gripper jaws (37-65 s), reopening the jaws (65-85 s), and returning to start position (85-120 s). In the contact scenario, an increase in light intensity (drop

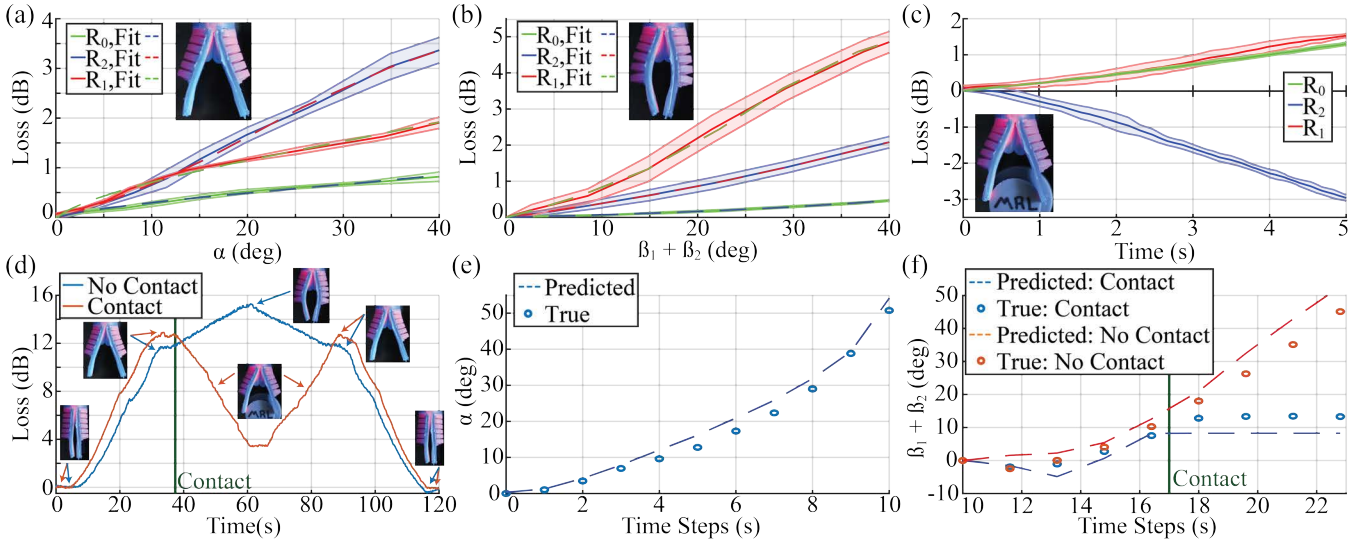

Fig. 7. Calibration testing of three soft robotic grippers with distinctly tuned sensor responses. Calibration of the light intensity change through the system during a) deployment, b) bending, and c) contact interactions of the gripper. The solid line is the mean value and the shaded area is one standard deviation. d) A comparison of the total loss in the ideal gripper (R_2) sensor during deployment and bending (with and without contacting an object). The subsequent control of the gripper (tracking tip position) is shown through the e) deployment of the gripper and f) highlighting the difference in the predicted response post contact compared to bending only (no contact).

in the loss or an optical gain) is observed when the gripper contacts an object (dark green line marks time of contact) between 37 and 65 s, thus indicating contact recognition and multi-modal sensing.

e) Ideal Roughness (R_2) Gripper Validation: The calibration data and fit equations gathered in Fig. 7, a-c are applied in the controls validation testing in Fig. 7, e-f on the ideally roughened gripper (R_2). The device fit is compared to the device's true position at subsequent steps of deployment with and without subsequent contact. Fig. 7, e shows the predicted deployment angle (same in contact and no contact scenarios tested). Fig. 7, f shows the contact recognition capabilities of the gripper as the predicted bending angle stays constant after contact.

B. Integrated Soft Robot Validation Experiment: Pick and Place Task with Shape Prediction and Contact Recognition

The soft robotic platform (robotic module with the ideally roughened gripper attached) was tested. The results of the test depict the ability of our system to track its position and shape within its workspace while moving to an object, picking it up, and moving it to another location.

The tracked positions of the system (via the WGs) are monitored and plotted in real-time and the results are shown in Fig. 8. We are able to accurately generate the shape of the robot from its base position (Fig. 8, a), through bending and deployment (Fig. 8, b-c), and monitor contact (Fig. 8, d). Please see the accompanying video.

V. Conclusions

We presented a fully soft robotic platform combining a soft optical sensorized multi-modal gripper for tip tracking and contact recognition and a multi-directional bending module with integrated 3D shape sensing. The multi-modal sensor embedded in the gripper is fabricated using roughness tuning on the CNC molds to control the sensor behavior. We have

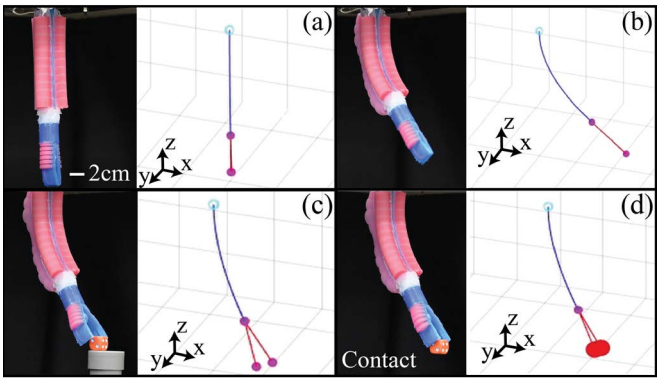

Fig. 8. Soft robotic platform validation testing showing different shape sensing predictions compared to the actual shape of the device as well as an example of contact recognition. a) The system in its base configuration. b) The system moving to the pick up location. c) The gripper deploys to pick up the object (i.e., a die). d) The gripper jaws contact the die and the system outputs this to the user by altering the visual output of the GUI.

validated the accuracy of our 3D shape sensing capabilities and the ability to distinguish between bending and contact of a gripper with a single WG sensor. The results of the robot module workspace testing exhibit the ability of our device to accurately determine its shape and tip location. Further, we characterized different roughness tuned WGs and determined that proper tuning can result in increased sensitivity across a range of curvatures and enhance optical gain characteristics without compromising sensor sensitivity in the loss direction. The multi-modal nature of the sensors integrated in the gripper allows for a reduced number of required sensors on the soft robot.

In its current implementation, the system cannot monitor the amplitude of contact forces. Future work will focus on implementing more sophisticated closed-loop control strategies via sensor integration from multiple sources, such as actuation pressures, to predict the magnitude of grasping contact interactions.

REFERENCES

[1] J. Shintake, V. Cacucciolo, D. Floreano, and H. Shea, "Soft Robotic Grippers," *Advanced Materials*, vol. 30, no. 29, 7 2018.

[2] J. Hughes, U. Culha, F. Giardina, F. Guenther, A. Rosendo, and F. Iida, "Soft manipulators and grippers: A review," *Frontiers Robotics AI*, vol. 3, no. NOV, 2016.

[3] P. Glick, S. A. Suresh, D. Ruffatto, M. Cutkosky, M. T. Tolley, and A. Parness, "A Soft Robotic Gripper with Gecko-Inspired Adhesive," *IEEE Robotics and Automation Letters*, vol. 3, no. 2, pp. 903–910, 4 2018.

[4] J. Zhou, S. Chen, and Z. Wang, "A Soft-Robotic Gripper with Enhanced Object Adaptation and Grasping Reliability," *IEEE Robotics and Automation Letters*, vol. 2, no. 4, pp. 2287–2293, 10 2017.

[5] V. Subramaniam, S. Jain, J. Agarwal, and P. Valdivia y Alvarado, "Design and characterization of a hybrid soft gripper with active palm pose control," *International Journal of Robotics Research*, vol. 39, no. 14, pp. 1668–1685, 12 2020.

[6] M. C. S. Yuen, T. R. Lear, H. Tonoyan, M. Telleria, and R. Kramer-Bottiglio, "Toward Closed-Loop Control of Pneumatic Grippers during Pack-and-Deploy Operations," *IEEE Robotics and Automation Letters*, vol. 3, no. 3, 2018.

[7] B. S. Homberg, R. K. Katzschmann, M. R. Dogar, and D. Rus, "Haptic identification of objects using a modular soft robotic gripper," in *IEEE International Conference on Intelligent Robots and Systems*, vol. 2015-December. Institute of Electrical and Electronics Engineers Inc., 12 2015, pp. 1698–1705.

[8] L. Chin, M. C. Yuen, J. Lipton, L. H. Trueba, R. Kramer-Bottiglio, and D. Rus, "A simple electric soft robotic gripper with high-deformation haptic feedback," in *Proceedings - IEEE International Conference on Robotics and Automation*, vol. 2019-May, 2019.

[9] R. Adam Bilodeau, E. L. White, and R. K. Kramer, "Monolithic fabrication of sensors and actuators in a soft robotic gripper," in *IEEE International Conference on Intelligent Robots and Systems*, vol. 2015-December. Institute of Electrical and Electronics Engineers Inc., 12 2015, pp. 2324–2329.

[10] F. Xu, H. Wang, W. Chen, and Y. Miao, "Visual Servoing of a Cable-Driven Soft Robot Manipulator with Shape Feature," *IEEE Robotics and Automation Letters*, vol. 6, no. 3, 2021.

[11] Y. She, S. Q. Liu, P. Yu, and E. Adelson, "Exoskeleton-covered soft finger with vision-based proprioception and tactile sensing," *IEEE International Conference on Robotics and Automation (ICRA)*, 10 2019.

[12] A. Yamaguchi and C. G. Atkeson, "Combining finger vision and optical tactile sensing: Reducing and handling errors while cutting vegetables," in *IEEE-RAS International Conference on Humanoid Robots*, 2016.

[13] H. A. Wurdemann, S. Sareh, A. Shafti, Y. Noh, A. Faragasso, D. S. Chathuranga, H. Liu, S. Hirai, and K. Althoefer, "Embedded electro-conductive yarn for shape sensing of soft robotic manipulators," in *Proceedings of the Annual International Conference of the IEEE Engineering in Medicine and Biology Society, EMBS*, vol. 2015-November, 2015.

[14] M. Luo, E. H. Skorina, W. Tao, F. Chen, S. Ozel, Y. Sun, and C. D. Onal, "Toward modular soft robotics: Proprioceptive curvature sensing and sliding-mode control of soft bidirectional bending modules," *Soft Robotics*, vol. 4, no. 2, pp. 117–125, 6 2017.

[15] M. Yang, Q. Liu, H. S. Naqawe, and M. P. Fok, "Movement detection in soft robotic gripper using sinusoidally embedded fiber optic sensor," *Sensors (Switzerland)*, vol. 20, no. 5, 2020.

[16] M. Amanzadeh, S. M. Aminossadati, M. S. Kizil, and A. D. Rakić, "Recent developments in fibre optic shape sensing," *Measurement: Journal of the International Measurement Confederation*, vol. 128, 2018.

[17] I. Floris, J. M. Adam, P. A. Calderón, and S. Sales, "Fiber Optic Shape Sensors: A comprehensive review," *Optics and Lasers in Engineering*, vol. 139, 2021.

[18] N. Rahman, N. J. Deaton, J. Sheng, S. S. Cheng, and J. P. Desai, "Modular FBG bending sensor for continuum neurosurgical robot," *IEEE Robotics and Automation Letters*, vol. 4, no. 2, pp. 1424–1430, 4 2019.

[19] K. C. Galloway, Y. Chen, E. Templeton, B. Rife, I. S. Godage, and E. J. Barth, "Fiber Optic Shape Sensing for Soft Robotics," *Soft Robotics*, vol. 6, no. 5, pp. 671–684, 10 2019.

[20] S. Russo, P. Dario, and A. Menciassi, "A novel robotic platform for laser-assisted transurethral surgery of the prostate," *IEEE Transactions on Biomedical Engineering*, 2015.

[21] C. Wu, X. Liu, and Y. Ying, "Soft and Stretchable Optical Waveguide: Light Delivery and Manipulation at Complex Biointerfaces Creating Unique Windows for On-Body Sensing," *ACS Sensors*, vol. 6, no. 4, 2021.

[22] W. Chen, C. Xiong, C. Liu, P. Li, and Y. Chen, "Fabrication and Dynamic Modeling of Bidirectional Bending Soft Actuator Integrated with Optical Waveguide Curvature Sensor," *Soft Robotics*, 3 2019.

[23] H. Krauss and K. Takemura, "Stretchable Optical Waveguide Sensor Capable of Two-Degree-of-Freedom Strain Sensing Mediated by a Semidivided Optical Core," *IEEE/ASME Transactions on Mechatronics*, 8 2022.

[24] M. McCandless, A. Gerald, A. Carroll, H. Aihara, and S. Russo, "A Soft Robotic Sleeve for Safer Colonoscopy Procedures," *IEEE Robotics and Automation Letters*, vol. 6, no. 3, pp. 5292–5299, 7 2021.

[25] A. Gerald, M. McCandless, A. Sheth, H. Aihara, and S. Russo, "A Soft Sensor for Bleeding Detection in Colonoscopies," *Advanced Intelligent Systems*, vol. 4, no. 4, 2022.

[26] A. Gerald, R. Batliwala, J. Ye, P. Hsu, H. Aihara, and S. Russo, "A Soft Robotic Haptic Feedback Glove for Colonoscopy Procedures," in *IEEE/RSJ International Conference on Intelligent Robots and Systems (IROS)*, 2022, pp. 583–590.

[27] Z. Zhang, Y. Zheng, J. Pan, X. Li, K. Li, Z. Zhang, X. Li, and K. Li, "A flexible dual-core optical waveguide sensor for simultaneous and continuous measurement of contact force and position," in *IEEE International Conference on Intelligent Robots and Systems*, 2020, pp. 7375–7380.

[28] Babar Jamil and Hugo Rodrigue, "Low-Powered and Resilient IR-Based Pigmented Soft Optoelectronic Sensors," *ACS Publications*, 2022.

[29] B. Jamil, J. Kim, and Y. Choi, "Force sensing fingertip with soft optical waveguides for robotic hands and grippers," in *2018 IEEE International Conference on Soft Robotics, RoboSoft 2018*. Institute of Electrical and Electronics Engineers Inc., 7 2018, pp. 146–151.

[30] H. Zhao, K. O'Brien, S. Li, and R. F. Shepherd, "Optoelectronically innervated soft prosthetic hand via stretchable optical waveguides," *Science Robotics*, vol. 1, no. 1, 2016.

[31] C. B. Teeple, K. P. Becker, and R. J. Wood, "Soft Curvature and Contact Force Sensors for Deep-Sea Grasping via Soft Optical Waveguides," *International Conference on Intelligent Robots and Systems (IROS)*, pp. 1621–1627, 2018.

[32] H. Zhao, R. Huang, and R. F. Shepherd, "Curvature control of soft orthotics via low cost solid-state optics," in *Proceedings - IEEE International Conference on Robotics and Automation*, vol. 2016-June, 2016, pp. 4008–4013.

[33] B. Jamil, G. Yoo, Y. Choi, and H. Rodrigue, "Proprioceptive Soft Pneumatic Gripper for Extreme Environments Using Hybrid Optical Fibers," *IEEE Robotics and Automation Letters*, vol. 6, no. 4, pp. 8694–8701, 10 2021.

[34] R. L. Truby, L. Chin, A. Zhang, and D. Rus, "Fluidic innervation sensorizes structures from a single build material," *Sci. Adv*, vol. 8, no. 32, p. 4385, 2022.

[35] J. Hughes, A. Spielberg, M. Chounlakone, G. Chang, W. Matusik, and D. Rus, "A Simple, Inexpensive, Wearable Glove with Hybrid Resistive-Pressure Sensors for Computational Sensing, Proprioception, and Task Identification," *Advanced Intelligent Systems*, vol. 2, no. 6, p. 2000002, 6 2020.

[36] N. Hanson, H. Hochsztein, A. Vaidya, J. Willick, K. Dorsey, and T. Padir, "In-Hand Object Recognition with Innervated Fiber Optic Spectroscopy for Soft Grippers," in *2022 IEEE 5th International Conference on Soft Robotics, RoboSoft 2022*, 2022, pp. 852–858.

[37] R. Kang, E. Guglielmino, L. Zullo, D. T. Branson, I. Godage, and D. G. Caldwell, "Embodiment design of soft continuum robots," *Advances in Mechanical Engineering*, vol. 8, no. 4, pp. 1–13, 4 2016.

[38] J. Lai, K. Huang, B. Lu, Q. Zhao, and H. Chu, "Verticalized-Tip Trajectory Tracking of A 3D-Printable Soft Continuum Robot: Enabling Surgical Blood Suction Automation," *IEEE/ASME Transactions on Mechatronics*, 2021.

[39] H. Bai, S. Li, J. Barreiros, Y. Tu, C. R. Pollock, and R. F. Shepherd, "Stretchable distributed fiber-optic sensors," *Science*, vol. 370, no. 6518, pp. 848–852, 2020.

[40] A. Hassan, F. Aljaber, H. Godaba, I. Vitanov, and K. Althoefer, "Soft Multi-point Waveguide Sensor for Proprioception and Extereoception

in Inflatable Fingers," in *6th International Forum on Research and Technology for Society and Industry, RTSI 2021 - Proceedings*, 2021, pp. 574–579.

[41] F. Aljaber, A. Hassan, I. Vitanov, and K. Althoefer, "Curvature and Contact Sensing with Optical Waveguides for Soft Silicone Pneumatic Actuator," in *2022 IEEE 5th International Conference on Soft Robotics, RoboSoft 2022*, 2022, pp. 859–864.

[42] R. J. Webster and B. A. Jones, "Design and kinematic modeling of constant curvature continuum robots: A review," *International Journal of Robotics Research*, vol. 29, no. 13, pp. 1661–1683, 11 2010.